Turbulent energy production and entrainment at a highly stratified estuarine front

Daniel G. MacDonald[1]

School for Marine Science and Technology, University of Massachusetts–Dartmouth, New Bedford, Massachusetts, USA

W. Rockwell Geyer

Woods Hole Oceanographic Institution, Woods Hole, Massachusetts, USA

Received 14 August 2003; revised 19 February 2004; accepted 4 March 2004; published 1 May 2004.

[1] Rates of turbulent kinetic energy (TKE) production and buoyancy flux in the region immediately seaward (~1 km) of a highly stratified estuarine front at the mouth of the Fraser River (British Columbia, Canada) are calculated using a control volume approach. The calculations are based on field data obtained from shipboard instrumentation, specifically velocity data from a ship mounted acoustic Doppler current profiler (ADCP), and salinity data from a towed conductivity-temperature-depth (CTD) unit. The results allow for the calculation of vertical velocities in the water column, and the total vertical transport of salt and momentum. The vertical turbulent transport quantities ($\overline{u'w'}$, $\overline{S'w'}$) can then be estimated as the difference between the total transport and the advective transport. Estimated production is on the order of 10^{-3} m^2 s^{-3}, yielding a value of $\varepsilon(\nu N^2)^{-1}$ on the order of 10^4. This rate of TKE production is at the upper limit of reported values for ocean and coastal environments. Flux Richardson numbers in this highly energetic system generally range from 0.15 to 0.2, with most mixing occurring at gradient Richardson numbers slightly less than $\frac{1}{4}$. These values compare favorably with other values in the literature that are associated with turbulence observations from regimes characterized by scales several orders of magnitude smaller than are present in the Fraser River. *INDEX TERMS:* 4546 Oceanography: Physical: Nearshore processes; 4568 Oceanography: Physical: Turbulence, diffusion, and mixing processes; 4235 Oceanography: General: Estuarine processes; *KEYWORDS:* turbulence, entrainment, estuary

Citation: MacDonald, D. G., and W. R. Geyer (2004), Turbulent energy production and entrainment at a highly stratified estuarine front, *J. Geophys. Res.*, *109*, C05004, doi:10.1029/2003JC002094.

1. Introduction

[2] Stratified shear flows become turbulent when the stabilizing influence of the stratification overcomes the velocity shear [*Thorpe*, 1971, 1973]. These flows can be found within the pycnocline in oceans, lakes, reservoirs, and estuaries as well as stratified regions of the atmosphere. The onset of turbulence in such flows greatly enhances vertical transport, affecting distributions of nutrients, sediments, and pollutants, as well as the dynamically important quantities of momentum and buoyancy. An understanding of these turbulent processes at scales relevant to geophysical flows is an important goal both for engineering applications in the natural environment and for a fundamental understanding of regional dynamics. Most investigations concerning the nature of shear-stratified turbulence, however, are based on laboratory experiments [e.g., *Ivey and Imberger*, 1991] or observations from relatively low-energy geophysical regimes [e.g., *Gregg*, 1989], due in large part to the difficulty involved in obtaining reliable measurements from more energetic oceanic environments [*Gargett and Moum*, 1995].

[3] As shown by *Ivey and Imberger* [1991], the status of the instantaneous energy budget of a turbulent field can be described by the overturn Froude number, $Fr_T = (L_O/L_t)^{\frac{2}{3}}$, and the overturn Reynolds number, $\mathrm{Re}_T = (L_t/L_K)^{\frac{4}{3}}$, where $L_O = (\varepsilon/N^3)^{\frac{1}{2}}$ is the Ozmidov scale, $L_K = (\nu^3/\varepsilon)^{\frac{1}{4}}$ is the Kolmogorov scale, and L_t is a representative turbulent length scale. Here ε represents the rate of dissipation of turbulent kinetic energy (TKE), ν is the kinematic viscosity of the fluid, and $N = \left(\frac{-g}{\rho_o}\frac{\partial \rho}{\partial z}\right)^{\frac{1}{2}}$ is the buoyancy frequency, where g represents gravity, ρ is the density of the fluid, and z is the vertical coordinate. The Ozmidov and Kolmogorov scales are fundamental length scales of the turbulent field, with L_O representing the largest eddy size that can be supported by a given turbulent dissipation rate within a region of specified stratification, and L_K defining the smallest turbulent scales, below which the turbulent energy is dissipated into heat. The overturn Reynolds

[1] Formerly at Massachusetts Institute of Technology/Woods Hole Oceanographic Institution Joint Program in Oceanography/Applied Ocean Science and Engineering, Woods Hole, Massachusetts, USA.

0148-0227/04/2003JC002094$09.00

number can also be written as $\mathrm{Re}_T = \frac{1}{Fr_T}\left(\frac{\varepsilon}{\nu N^2}\right)$, and the expression $\left(\frac{\varepsilon}{\nu N^2}\right)$ is commonly used as a normalized expression for dissipation.

[4] If a turbulent field can be assumed homogeneous and isotropic, then the advection of TKE can be neglected, and the flux Richardson number can be defined as $Ri_f = \frac{B}{P}$. This ratio represents the fraction of TKE generated from shear production, P, that is converted to potential energy through positive buoyancy flux, B. A clear understanding of the nature of Ri_f is critical for developing estimates of eddy diffusivity from observations of turbulent dissipation, as discussed by *Osborn* [1980], who suggested that Ri_f should be equal to 0.15 based on observations of oceanic turbulence. *Ivey and Imberger* [1991] similarly suggested a range between 0.15 and 0.2 based on laboratory flows characterized by values of $\frac{\varepsilon}{\nu N^2}$ between approximately 10 and 100, with an overturn Froude number equal to 1. An overturn Froude number equal to 1 is consistent with most oceanic thermocline measurements [*Gregg*, 1987; *Peters et al.*, 1988], where Kelvin-Helmholz billows are believed to be the primary mechanism of turbulence generation. Their laboratory data also indicated that Ri_f should fall off rapidly with increases in both parameters, $\frac{\varepsilon}{\nu N^2}$ and Fr_T. Recent observations of atmospheric boundary layer turbulence [*Pardyjak et al.*, 2002] have indicated Ri_f values of approximately 0.2 for flows with gradient Richardson numbers $\left[Ri_g = N^2\left(\frac{\partial u}{\partial z}\right)^2\right]$ near the critical value of $\frac{1}{4}$, and values of $\frac{\varepsilon}{\nu N^2}$ on the order of 10^5. Similarly, *Kay and Jay* [2003a] have observed values of Ri_f between 0.18 and 0.26 along a saline interface in the highly stratified Columbia River estuary during ebb tide, characterized by $\frac{\varepsilon}{\nu N^2}$ values on the order of 10^4 to 10^5.

[5] Some recent studies have suggested values of the flux Richardson number outside of the 0.15 to 0.2 range. *Gargett and Moum* [1995] report Ri_f values as high as 0.4 associated with shear produced turbulence at a highly energetic tidal front. Conversely, *Barry et al.* [2001a, 2001b] suggest that the mixing efficiency for laboratory generated grid turbulence may decrease to zero for $\frac{\varepsilon}{\nu N^2} > 1000$, coincident with an increase in the overturn Froude number. Similar results have been observed in DNS simulations performed by *Ivey et al.* [1998]. Field observations of the interior of two stratified lakes, where turbulence is driven mainly by internal wave breaking, found negligible mixing efficiencies at $\frac{\varepsilon}{\nu N^2}$ values ranging from 10^{-1} to 10^3 [*Etemad-Shahidi and Imberger*, 2001], and similar conditions have been observed in the oceanic thermocline [*Moum*, 1996]. Etemad-Shahidi and Imberger suggest that the differences between these results and earlier laboratory studies are due to differences in the mechanisms triggering the turbulence. Similarly, *Balmforth et al.* [1998] have suggested that grid-generated turbulence may not be representative of shear-produced turbulence.

[6] This brief review suggests that there is considerable variability among existing observations of Ri_f. In 1991, *Imberger and Ivey* [1991] recognized that a "strong debate" had been underway for several years regarding the magnitude of Ri_f. Despite significant effort over the last decade, this debate remains unresolved, particularly for highly energetic flows.

[7] The classic estuarine outflow is characterized by a stratified shear flow, providing an ideal setting for investigating stratified shear turbulence. Seaward of an estuarine front, the fresh water outflow thins in the vertical and expands laterally [*Kashiwamura and Yoshida*, 1967, 1972], resulting in a shear-enhancing flow acceleration, as shown in Figure 1. *Wright and Coleman* [1971] identified the importance of vertical mixing to flows of this type through an observational study of the Mississippi River outflow. Although the upper layer acceleration, which ultimately drives the shear-induced mixing processes, may be controlled by the availability for plume expansion, locally valid relationships must control the rate of TKE production, and the flux Richardson number.

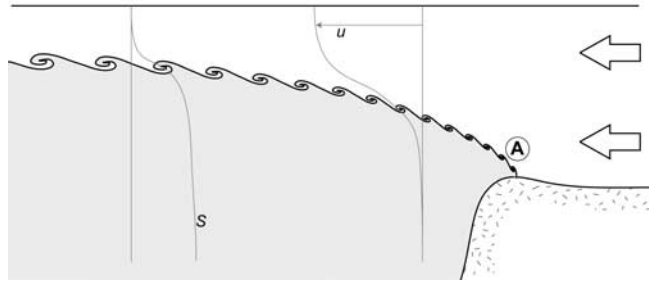

Figure 1. Definition sketch of an estuarine outflow. Fresh (S = 0) river water discharges from the right. Seaward of the salt front at point A, the fresh water layer thins in the vertical, and may expand laterally in the direction perpendicular to the page. The flow accelerates through this transition region, increasing vertical shear and triggering Kelvin-Helmholtz-like flow instabilities and turbulent mixing. Representative profiles of along channel velocity, u, and salinity, S, are shown for reference.

[8] Accurate TKE measurements in highly energetic estuarine outflows can be difficult to obtain. Traditional measurements using microstructure profilers [e.g., *Gargett and Moum*, 1995; *Peters*, 1999] and alternative measurements, such as acoustic Doppler current profiler (ADCP) variance techniques [*Stacey et al.*, 1999], are all subject to implementation constraints in the highly sheared environment. In this paper, a control volume method utilizing conductivity-temperature-depth (CTD) and ADCP data is described and used to obtain estimates of the vertical structure of TKE production and buoyancy flux at the highly stratified mouth of the Fraser River (British Columbia, Canada). Section 2 discusses the specifics of the observational program, followed by presentation of the control volume method and TKE results in section 3. Implications of the observed TKE values, in the context of estuarine outflows, are discussed in section 4, with a summary of pertinent conclusions presented in section 5.

2. Observational Program

[9] The study was conducted at the mouth of the Fraser River, in southwestern British Columbia, Canada (Figure 2). The dynamics in the estuary are dominated by an interaction between the local tides and the freshwater discharge. Tides in the Strait of Georgia are mixed semidiurnal and diurnal, with amplitudes typically ranging from 2.5 to 4 m, and tidal velocities on the order of

Figure 2. Locus of the Fraser River Estuary, British Columbia, Canada.

1 m s^{-1}. River discharge is dominated by the summer freshet, during which discharge typically increases by a factor of 10 relative to low flow, and net outflow velocities reach 0.5 to 1 m s^{-1}. The highly energetic estuarine environment generated through the interaction of these two strong forcing mechanisms results in the formation of a salt wedge with salinity differences of greater than 20 psu across only a few meters in the vertical and less than 500 m in the horizontal. This salt wedge advances landward some 10 to 20 km into the channel on each tidal cycle, only to be flushed back to the mouth daily during the strong ebb [*Geyer and Farmer*, 1989]. The front location remains nearly stationary at the mouth for several hours prior to advancing again on the following flood. During this period, the front is positioned just landward of a distinct bathymetric break, which transects the channel at an angle of approximately 45°, separating channel depths on the order of 10 m from bathymetry exceeding 50 m in the Strait of Georgia. The analyses presented here focus on the frontal zone during this stationary period.

[10] The data evaluated in this study was collected on July 25, 1999, 5 days past neap tide. River discharge on July 25 was approximately 7500 m^3 s^{-1}, as measured at the most seaward gauging station, located at Hope, approximately 150 km upstream of the mouth. Data were collected from the R/V *Clifford Barnes* (University of Washington), using two hull-mounted ADCPs, operating at 1200 kHz and 300 kHz, and a "tow-yoed" Ocean Sensors 200 Series CTD unit. Combined use of the two ADCPs allowed for consistent bottom tracking coupled with a vertical resolution on the order of 25 cm across the top 25 m of the water column. Vertical resolution of the CTD unit was on the order of 5 to 10 cm. Data were collected from repeated passes across the front as shown in Figure 3.

[11] Data from the passes indicate strong stratification and convective acceleration across the front, as shown in Figure 4. The bold lines in the figure represent mean "freshwater streamlines," and indicate the bounding surfaces for specific fractions of the original river discharge. These surfaces were estimated based on fresh water conservation, assuming a salinity of pure Georgia Strait water of S_o = 27 psu,

$$Q_o = \int_{z_{S_o}}^{0} u \frac{(S_o - S)}{S_o} b dz, \tag{1}$$

where Q_o is constant and equal to the total fresh water flux in the cross section, u is the velocity parallel to a mean upper layer flow direction (defined as the x direction), S is the local salinity, and $b = b(x, z)$ is a plume width in the cross-stream direction. Using equation (1) and some simple assumptions regarding the shape of the vertical profile of b, the trajectory of fresh water streamlines can be evaluated. Sensitivity to the shape of the b profile was tested by performing multiple calculations using a variety of profiles, including width profiles that were constant, linear, and parabolic with depth. The angle of the freshwater streamlines relative to the isohalines shows that the initially fresh discharge becomes progressively more saline through the liftoff zone. This can only be accomplished through the diffusive effects of turbulent mixing.

3. Estimation of Turbulent Fluxes

[12] The control volume analysis used for the estimation of turbulent transport quantities relies on three conservation constraints: volume, salt, and momentum. The three resolved unknowns include the mean velocity normal to the bottom surface of the control volume and the vertical turbulent transport of salt and momentum. The results of the turbulent flux calculations for salt and momentum are independent of the choice of the control volume, but the calculated velocity across the bottom surface of the control volume is reference frame dependent, based on the orientation of the surface, as described in Appendix A. Here we

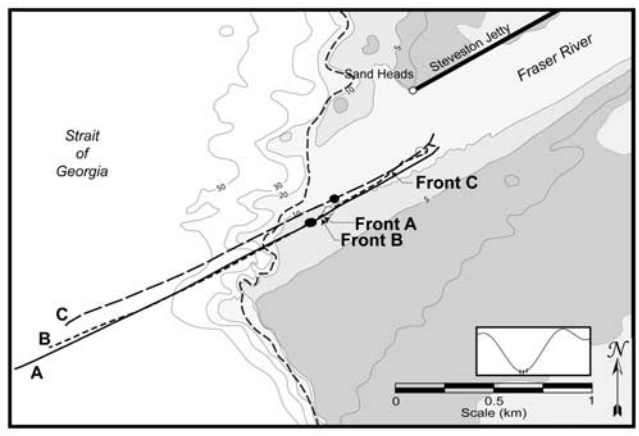

Figure 3. Plan view of estuary mouth, showing ship tracks of three passes during low tide on July 25, 1999. Dashed line represents the 12-m isobath, approximating the location of the bathymetric break. Observed location of the front during each pass is indicated by the open and closed circles, representative of the absence of 14 psu salinity fluid, and the presence of 14 psu salinity fluid, respectively.

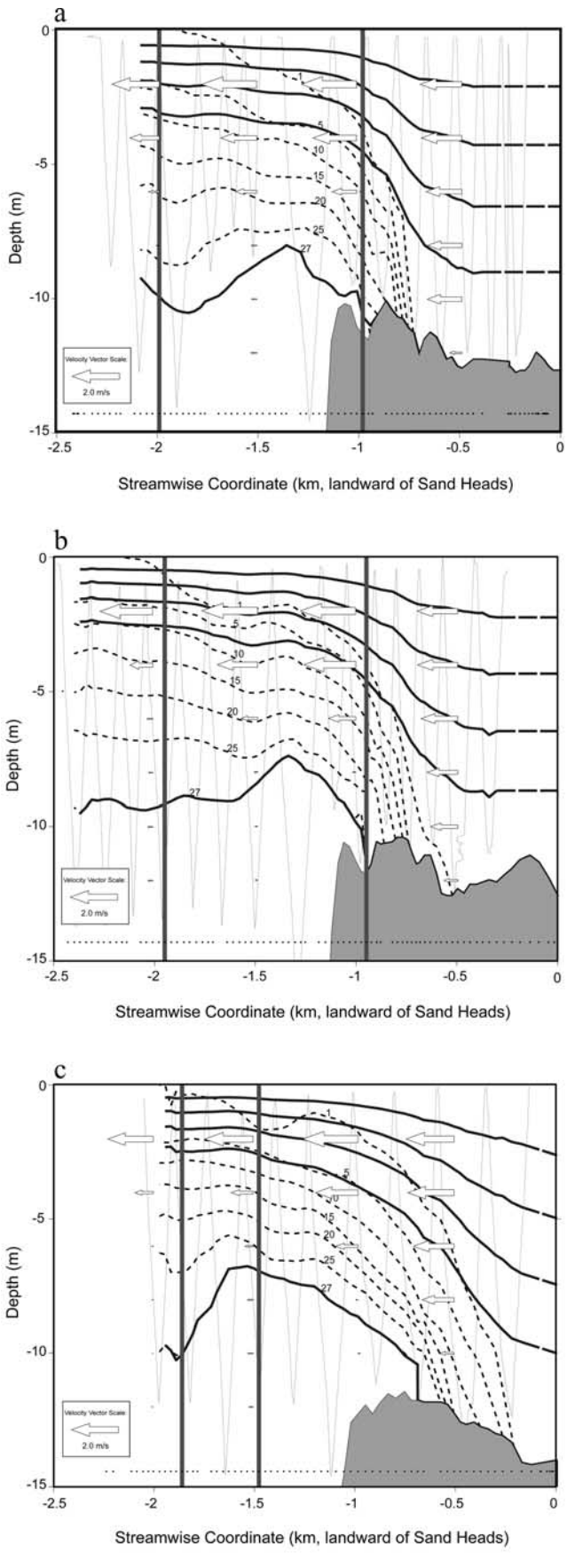

will calculate two quasi-vertical velocities, the diahaline velocity, w_h, taken relative to isohaline surfaces, and the "jet-entrainment" velocity, w_j, taken relative to freshwater streamlines.

[13] Volume conservation is used to identify the mean velocity across the bottom control volume surface. Written as an integral across the control volume surface, this can be expressed as

$$\iint_{C\,S} \vec{U} \cdot d\vec{A} = \frac{\partial V}{\partial t}, \tag{2}$$

where $\vec{U}$ represents the local velocity at the control volume surface, $\vec{A}$ is a unit vector perpendicular to the surface, the integral represents summation over the entire control volume surface, and V is the total volume contained within the control surface. Assuming no contribution from lateral fluxes (an assumption that will be discussed in further detail below and in Appendix B), the control volume continuity equation can be rewritten in differential form as

$$\frac{\partial}{\partial x}\left[\int budz\right] + \bar{w}b = \frac{\partial}{\partial t}\left[\iint bdz\right], \tag{3}$$

where the integrals are taken across the limits of the control volume, and $\bar{w}$ represents the mean velocity normal to the bottom surface of the control volume, which is equal to w_h if the bottom control volume surface is coincident with an isohaline, or w_j if aligned with a freshwater streamline.

[14] A similar treatment of the salt balance allows for estimation of the total vertical salt flux, $\overline{Sw}$, starting with an expression for the integrated salt balance,

$$\iint_{C\,S} S\vec{U} \cdot d\vec{A} = \frac{\partial}{\partial t}\left[\iiint_{C\,V} SdV\right], \tag{4}$$

with salinity represented by S. This can be written in differential form as

$$\frac{\partial}{\partial x}\left[\int Sbudz\right] - \overline{Sw}b = -\frac{\partial}{\partial t}\left[\iint Sbdz\right]. \tag{5}$$

Once an estimate of the total vertical salt flux has been generated, the turbulent part can be extracted following a Reynolds decomposition, and making use of the quasi-vertical velocity estimated in equation (2),

$$\overline{S'w'} = \overline{Sw} - \bar{S}\bar{w}, \tag{6}$$

where $\bar{S}$ is the mean salinity of the bottom control volume surface. If the bottom surface is coincident with an

Figure 4. Cross section through the front for the three passes, (a) A, (b) B, and (c) C. Dashed contours represent salinity, in psu. Arrows represent streamwise velocity, based on the scale in the lower left-hand corner of the figure. Bold solid lines are freshwater streamlines, calculated through the conservation of freshwater as described in the text. CTD tow-yo track is shown in the background of each figure, and ADCP profile locations are identified by the dots near the bottom of each panel. Regions used for control volume analyses are delineated by the two vertical lines.

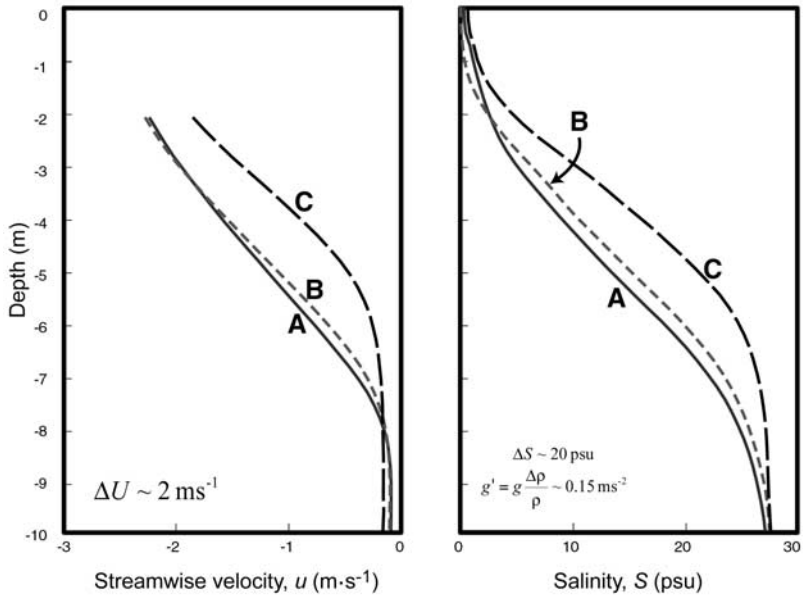

Figure 5. Vertical profiles of measured quantities, velocity and salinity, in the control volume region for each of the three lift-off passes. Plots represent mean profiles across the control volume region, which has a streamwise dimension of approximately 1 km for passes A and B, and approximately 400 m for pass C.

isohaline, $\bar{S}$ is equal to the salinity associated with the isohaline.

[15] Treatment of the momentum balance requires knowledge of the net force on the control volume associated with the local pressure, but is otherwise similar to the salt balance. Estimation of the turbulent momentum flux can be represented by the integrated and differential forms of the momentum equation,

$$\sum F_x = \iint_{C\,S} u\rho\vec{U}\cdot d\vec{A} + \frac{\partial}{\partial t}\left[\iiint_{C\,V} u\rho dV\right], \tag{7}$$

$$g\frac{\partial}{\partial x}\left(\int b\left[\frac{1}{\rho_o}\int \rho dz + \eta\right]dz\right) + \frac{\partial}{\partial x}\left[\int bu^2 dz\right] - \overline{uw}b = -\frac{\partial}{\partial t}\left[\int\int ubdz\right], \tag{8}$$

$$\overline{u'w'} = \overline{uw} - \bar{u}\bar{w}, \tag{9}$$

where F_x represents force in the streamwise direction associated with the local pressure, and η is the local surface displacement.

[16] This analysis method is similar in many respects to the "method of constrained differences" described by *Kay and Jay* [2003b], but utilizes an array of spatially distributed data instead of profiles from a single location. This distinction is important for the present case, as convective acceleration plays a key role in the momentum balance due to the rapid rise of the pycnocline through the lift-off zone. The convective acceleration term can be adequately constrained only through an appropriate spatial analysis.

[17] The size of the control volumes used for the analyses was on the order of 0.5 to 1 km in the x direction (as identified in Figure 4). The top control volume surface was always taken coincident with the water surface, so that the quasi-vertical fluxes would be directed only across the lower control volume boundary. The orientation of the lower boundary, across which turbulent fluxes and normal velocities are calculated, varied depending on the nature of the conservation calculation (i.e., volume, salt, or momentum). Although the calculations outlined above are viable for any defined volume, so that a standard set of boundary surfaces could be used for all calculations, it is preferable to use separate boundary surfaces associated with each process for a variety of reasons. For the diahaline velocity and turbulent salt flux estimates, a lower boundary represented by isohalines was used. Not only was this a natural choice for calculations involving salt flux, but the tighter spacing of isohalines near the base of the plume provided a higher resolution in this region where the majority of salt flux occurs. Alternatively, freshwater streamlines were used to identify the jet-entrainment velocity profiles and turbulent momentum flux calculations. The freshwater streamline concept provides a natural reference frame for further calculations involving momentum fluxes, particularly in the present case, where momentum enters the system associated with the fresh river discharge. This choice provides enhanced resolution of momentum fluxes near the surface, where there are strongly sheared velocities, and strong gradients in the turbulent flux of streamwise momentum. Time-dependent terms were estimated by comparing subsequent passes, but were generally small.

[18] Mean velocity and salinity profiles for the three passes, representing the two independent variables in the shear-stratified environment, are presented in Figure 5. The highly sheared streamwise velocity profiles are presented in the first panel, with values of Δu on the order of 2 m s^{-1}. Likewise, the salinity profiles identify a zone

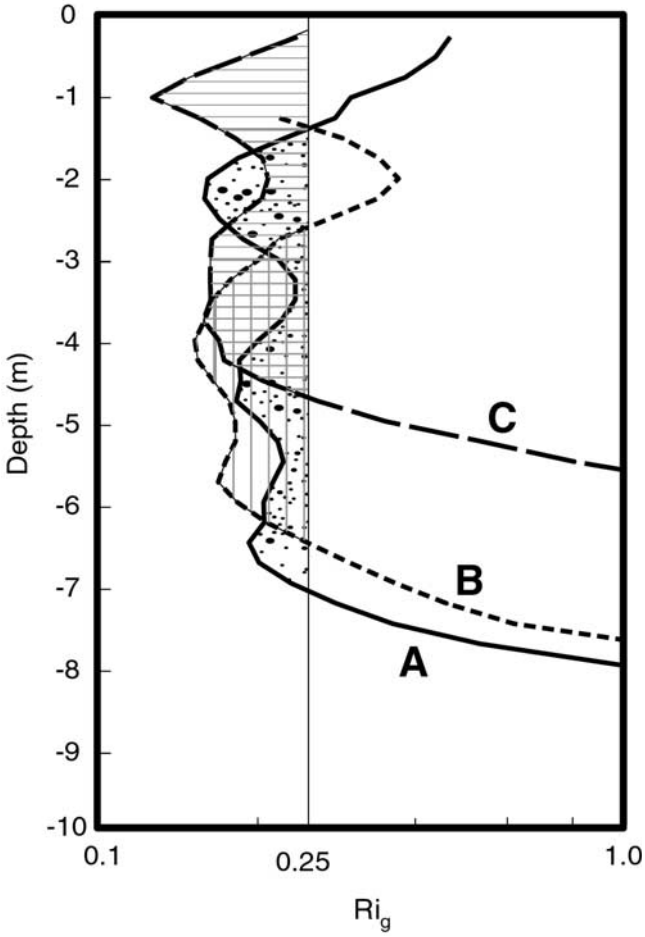

Figure 6. Vertical profiles of the gradient Richardson number, based on the mean quantities shown in Figure 5. Profiles are smoothed across approximately 1.5 m in the vertical. The vertical line represents a value of 1/4, and the shaded regions indicate the locations where the gradient Richardson number is less than $\frac{1}{4}$.

of strong stratification between roughly 3 and 8 m below the surface, with a value of ΔS on the order of 20 psu, and a corresponding $g' = g\Delta\rho(\rho_o)^{-1}$ value of approximately 0.15 m s^{-2}. Profiles of the gradient Richardson number based on the mean profiles of Figure 5 are shown in Figure 6. Much of the shear layer has values of Ri_g less than 0.25.

3.1. Volume Conservation and Vertical Entrainment Velocity

[19] Diahaline and jet-entrainment velocities were calculated using the method described by equations (2) and (3), above, utilizing isohalines and freshwater streamlines, respectively, as bounding surfaces for the control volumes. Mean vertical profiles of w_h and w_j for each of the passes are presented in the two panels of Figure 7. Error ranges shown in Figure 7 represent the standard deviation of the results associated with five different assumptions regarding the vertical shape of the plume width function, b. This error is negligible at depths less than approximately five meters, and generally less than 30% at depth. The profiles of w_h in the panel at the left show entrainment of both surface and deep water into a developing mixed layer centered at approximately 3 to 4 m depth and approximately 10 to 14 psu. In the panel on the right, the profiles of w_j indicate that ambient fluid is being entrained into all portions of the initial discharging plume, with higher velocities at depth. At the bounding limit of the plume, w_h is equal to w_j because the lowest streamline of the expanding discharge is coincident with the 27 psu isohaline.

3.2. Salt Conservation

[20] Total vertical salt transport is calculated as described above, utilizing a series of isohaline surfaces as the bottom control volume surface. The first panel of Figure 8 shows profiles of turbulent salt flux, expressed as buoyancy flux,

$$B = g\beta\overline{S'w'}, \tag{10}$$

where $\beta = \left(\frac{1}{\rho}\frac{\partial\rho}{\partial S}\right) = 0.77 \times 10^{-3}$ psu^{-1}. In the second panel, profiles of eddy diffusivity, derived from the turbulent salt flux profiles $\left[K_z^\rho = -\overline{\rho'w'}\left(\frac{\partial\rho}{\partial z}\right)^{-1}\right]$ are plotted. The buoyancy flux profiles are similar for the three passes, which peak near 2×10^{-4} m^2 s^{-3} in the middle of the pycnocline near 4 m depth. The profiles of eddy diffusivity indicate values of K_{z^ρ} on the order of 2 to 6×10^{-3} m^2 s^{-1} across the middle portion of the water column. The negative values of both buoyancy flux and eddy diffusivity observed below about 8 m for pass B are unrealistic, and are most likely explained by unresolved lateral influxes of salt and volume.

3.3. Momentum Conservation

[21] The procedure for calculation of the total vertical momentum flux requires an estimate of net streamwise force on the control volume. A hydrostatic force balance is assumed, and the baroclinic contribution is estimated from density profiles within the control volume. The barotropic contribution is determined from a surface gradient, $\partial\eta/\partial x$, estimated as the gradient required to produce a layer of no motion, as observed at depths sufficiently below the plume. The reference level for this layer was typically taken at 10 m below the surface, in order to extend the control volumes landward of the bathymetric break. In most cases, the 10 m depth was sufficiently deep to satisfy the no motion assumptions, but in the case of pass C the assumptions were invalidated due to weak landward currents in the lower layer near the front. In this case, the control volume region was shortened and moved offshore, as shown in Figure 4. Alternative approaches to estimating surface slope include the assumption that there is no stress divergence at the water surface, in which case the Bernoulli equation is valid (i.e., $\eta = \frac{1}{2g}u^2 + \frac{1}{g}\int\frac{\partial u}{\partial t}dx$). Another approach is to invoke zero momentum flux across the lower boundary of the plume (defined as the 100% fresh water streamline). The surface elevation profile must then force a stepwise control volume calculation of turbulent momentum flux to zero at the lower boundary. Profiles of the surface elevation, η, are shown in Figure 9, where the layer of no motion estimate is compared with the Bernoulli and zero momentum transport alternatives. Note the general consistency between the three estimates over their range of overlap.

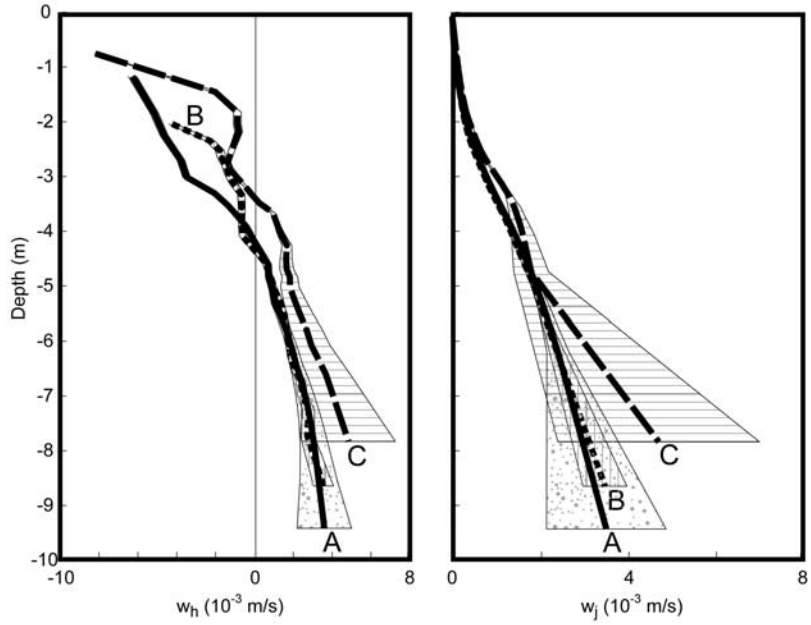

Figure 7. Vertical profiles of the mean vertical velocities, w_h and w_j, as calculated from the control volume analyses. Estimates are bracketed by error bounds, based on the standard deviation of the results using five different width assumptions.

The water surface exhibits its steepest gradient across the frontal zone, where there is a significant conversion of potential to kinetic energy associated with acceleration in the plume.

[22] Profiles of turbulent momentum flux, $\overline{u'w'}$, are shown in Figure 10. These profiles peak between approximately 2 and 5 m below the surface at values on the order of 1 to 2 $\times$ 10^{-3} m^2 s^{-2}. In Figure 11 vertical profiles for two quantities derived from the turbulent momentum flux are shown. In the first panel, profiles of TKE production are plotted, calculated as the product of the turbulent momentum flux and the local shear,

$$P = -\overline{u'w'}\frac{\partial u}{\partial z}. \tag{11}$$

These profiles are similar in shape to the turbulent momentum flux profiles, with production peaking at values

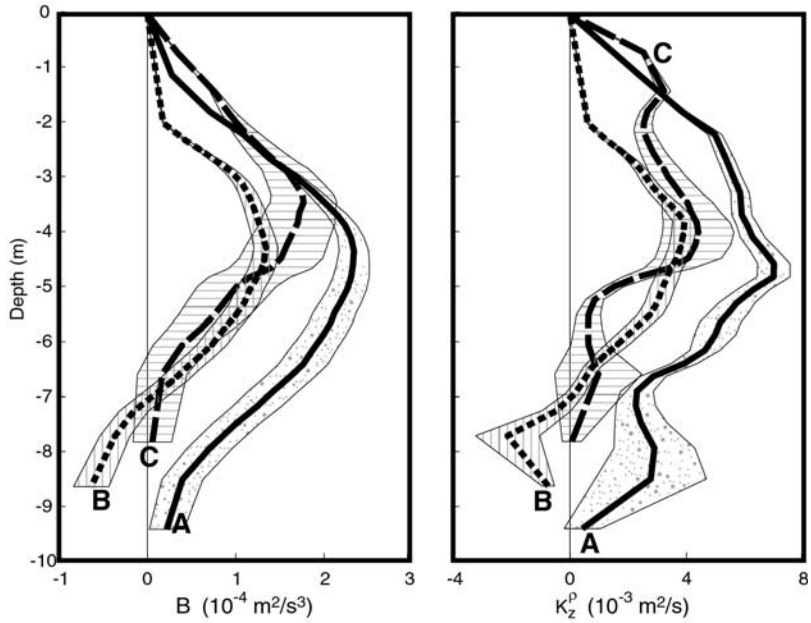

Figure 8. Buoyancy flux (B), and eddy diffusivity (K_z^ρ) profiles from control volume analysis. Each estimate is bracketed by standard deviation as in Figure 7. Note that estimates below approximately 5 to 6 m are also influenced by unresolved lateral fluxes as discussed in the text.

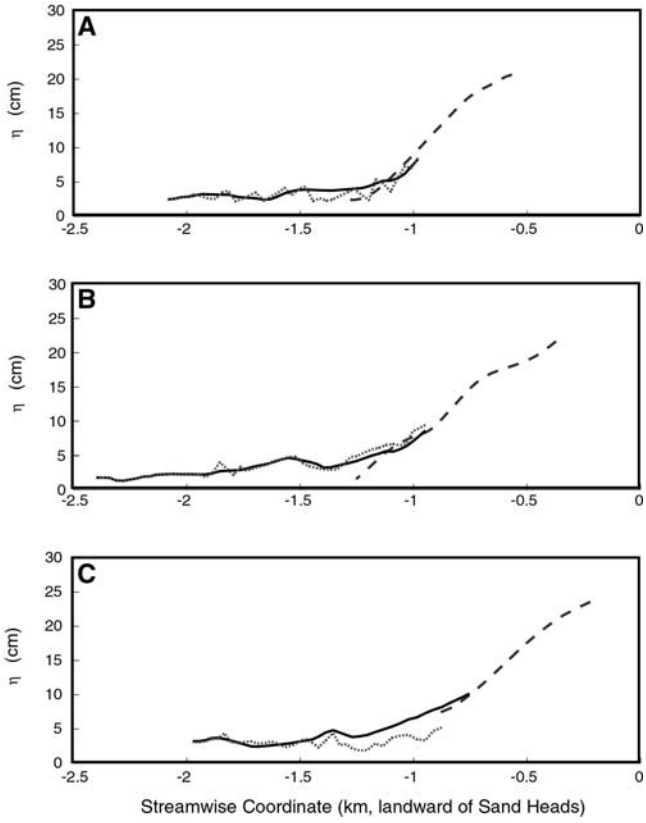

Figure 9. Estimates of surface elevation across the lift-off region based on three different methods of estimating the surface slope, $\partial\eta/\partial x$. The solid line represents the assumption of a layer of no motion, and zero stress divergence at a depth of 10 m below the surface. These results were used for subsequent momentum budget calculations. The dotted line represents the surface profile required to force the stress to zero at depth ($\sim$15 m below the surface) using a modified form of the control volume analysis. The dashed profile was derived using a Bernoulli approach based on the extrapolated surface velocities, assuming zero stress divergence at the surface. The dashed profile is terminated in the seaward direction where surface salinities exceeded 1 psu, providing evidence of mixing and an invalidation of the zero stress divergence assumption.

on the order of 0.5 to 1 $\times$ 10^{-3} m^2 s^{-3}. Profiles of eddy viscosity $\left[K_z^u = -\overline{u'w'}\left(\frac{\partial u}{\partial z}\right)^{-1}\right]$ are shown in the second panel. These profiles are consistent in shape and magnitude with the profiles of eddy diffusivity shown in Figure 8, except near the base of the pycnocline, where the momentum flux estimates are less reliable.

[23] Estimates of the dissipation rate can be generated, assuming that the turbulent field is isotropic and homogeneous, by taking the difference between the production and buoyancy flux profiles shown in Figures 11 and 8, respectively. These profiles are shown in Figure 12, along with corresponding profiles of $\frac{\varepsilon}{\nu N^2}$. These results place the magnitude of the dissipation rate in the Fraser lift-off zone on the order of 10^{-3} m^2 s^{-3}. Associated values of $\frac{\varepsilon}{\nu N^2}$ are on the order of 10^4.

3.4. Lateral Effects

[24] A potential source of error to the control volume calculations is the lateral flux of volume, salt and momentum. A separate analysis of the importance of these errors was performed using the observed cross-channel velocity structure and an estimated cross-channel length scale, as described in Appendix B. In all cases, lateral flux contributions tend to be negligible in the upper portion of the water column but may increase rapidly below approximately 5 to 6 m, toward values on the order of the contributions of vertical advective and turbulent fluxes to the momentum and salt balances. Calculations in the upper water column are relatively unaffected by lateral fluxes due to the alignment of the streamwise direction with the mean upper layer flow direction. Further discussion of the control volume results is limited to those within the upper region of the water column where errors associated with lateral fluxes are small.

4. Turbulence, Entrainment, and Closure

[25] The turbulent quantities estimated in section 3 were derived from mean flow quantities by closing budgets of volume, salt, and momentum. Owing to the nature of the calculations, individual fluctuating quantities were not estimated independently, but only as turbulent fluxes, represented by correlations (e.g., $\overline{S'w'}$). The estimated turbulent quantities represent means over the observation period, and across the length of the control volume, which was generally between 0.5 to 1 km. The observation period was equal to the time required for the observation vessel to transit along the length of the control volume, which ranged from 3 to 7 min.

[26] The TKE dissipation rates shown in Figure 12 represent a large amount of turbulent energy in comparison to other studies from ocean and coastal environments. For

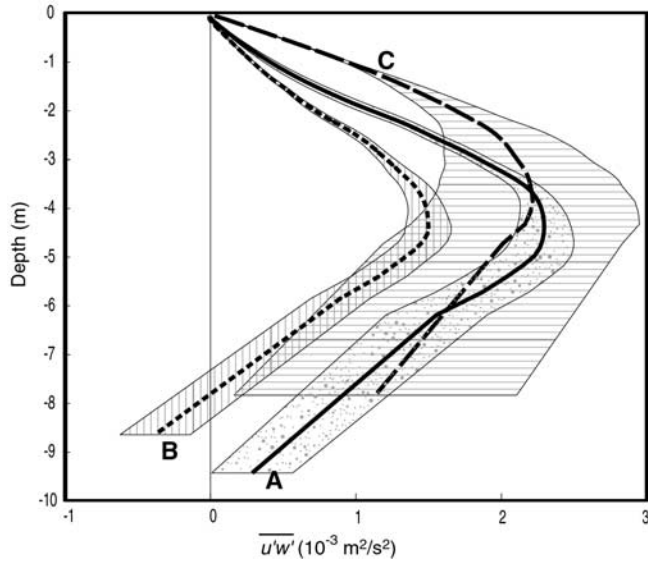

Figure 10. Turbulent momentum flux ($\overline{u'w'}$) profiles from control volume analysis. Each estimate is bracketed by standard deviation as in Figure 7. Note that estimates below approximately 5 to 6 m are influenced by unresolved lateral fluxes as discussed in the text.

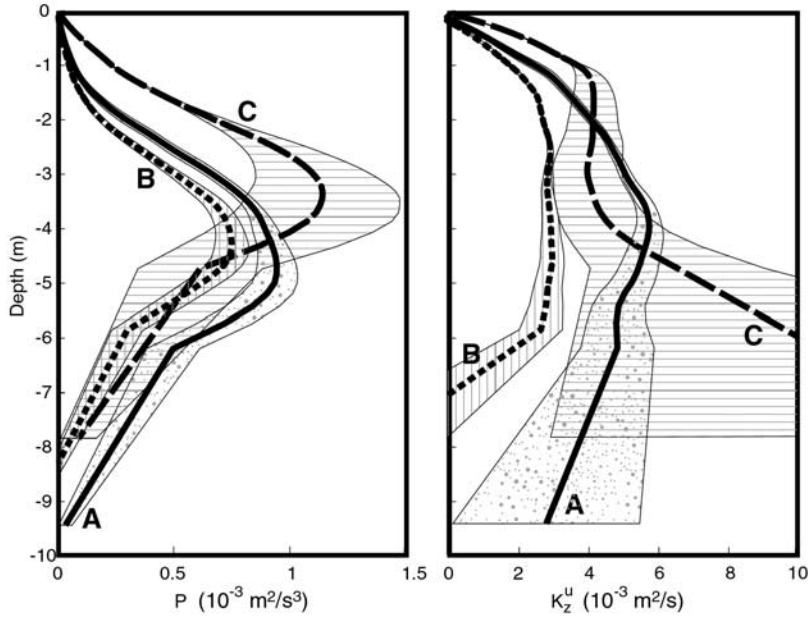

Figure 11. TKE production (P), and eddy viscosity (K_z^u) profiles from control volume analyses. Each estimate is bracketed by standard deviation as in Figure 7. Note that estimates below approximately 5 to 6 m are also influenced by unresolved lateral fluxes as discussed in the text. Eddy viscosity profiles for passes B and C exceed the bounding limits of the plot at depth. The scale was constrained to provide enhanced detail in the central portion of the water column.

example, *Gregg* [1989] reports that dissipation rates within the oceanic thermocline typically fall within a range of order 10^{-10} to 10^{-6} m^2 s^{-3}. Higher rates have been observed in tidal channels and in estuaries, but rarely exceeding 10^{-4} m^2 s^{-3}, and typically several orders of magnitude lower [see *Grant et al.*, 1962; *Gargett and Moum*, 1995; *Peters*, 1999]. Corresponding values of turbulent eddy diffusivities are on the order of 0.5×10^{-2} m^2 s^{-1}, as shown in Figures 8 and 11. These values are more typical of observed K_z values in ocean and coastal environments [e.g., *Ledwell et al.*, 1993; *Osborn*, 1980], due to the intense stratification present. The large values of dissipation relative

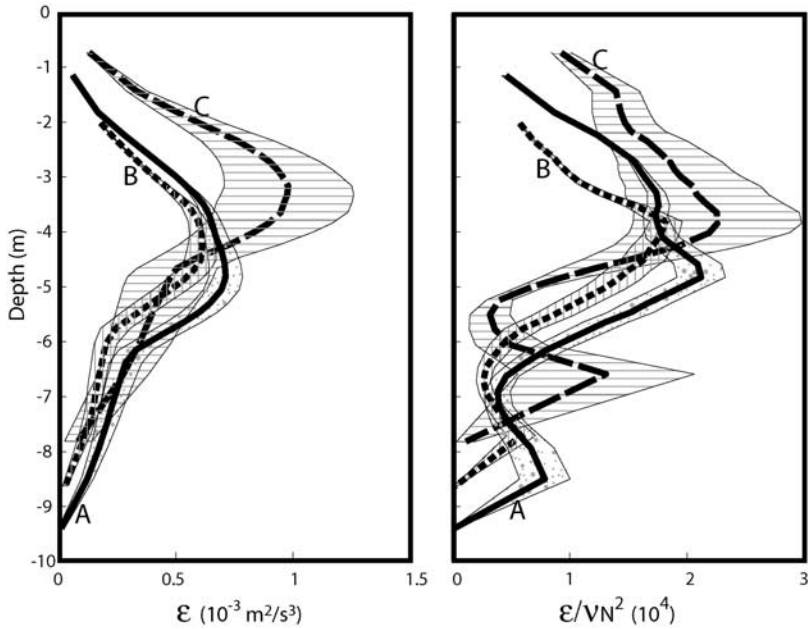

Figure 12. TKE dissipation (ε), and $\varepsilon/\nu N^2$ profiles derived from production and buoyancy flux estimates shown in Figures 11 and 8, respectively. Each estimate is bracketed by standard deviation as in Figure 7, and subject to unresolved lateral fluxes below approximately 5 to 6 m, as discussed in the text.

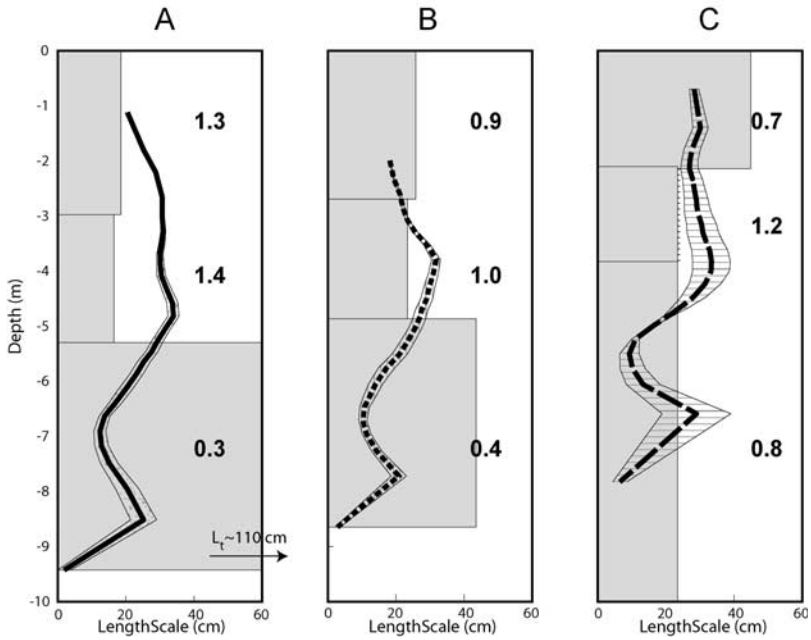

Figure 13. Profiles of Ozmidov scale, L_O, for each of the three passes based on the dissipation profiles shown in Figure 12, and the stratification shown in Figure 5. Each estimate is bracketed by standard deviation as in previous figures. Shaded horizontal bars represent mean observed overturn scales, L_T, for three salinity ranges: 0–5, 5–15, and >15 psu. Note that the observed overturn scale for the >15 psu range for Pass A extends beyond the range of the axes. Bold numbers represent the mean value of the overturn Froude number, $Fr_T = (L_O/L_T)^{\frac{2}{3}}$ within each of the regions.

to diffusivity are explained by the unusually strong vertical density gradients in the frontal zone.

[27] A third expression of turbulent intensity, and one that can be corroborated with independent observations, is the outer length scale of the turbulence, represented by the Ozmidov scale, and the corresponding observed overturn scale. In general, Ozmidov scales associated with the three passes ranged from 15 to 35 cm. Profiles of the local Ozmidov scale for each of the three passes are shown in Figure 13, compared with observed overturn scales [*Thorpe*, 1977] for three distinct regions associated with each pass, as represented by the shaded bars. The overturn scales shown here were calculated as the RMS value of all non-zero displacements observed within each region (0–5, 5–15, and >15 psu). Representative overturn Froude numbers for each region, based on the observed Ozmidov and overturn scales, are also shown in Figure 13.

[28] Within the middle region (5–15 psu), where there is linear shear and stratification, and the control volume estimates are reliable, the Ozmidov and overturn scales suggest an overturn Froude number on the order of 1.0 to 1.4. Although the exact value of this ratio may be a function of the evolution of the turbulence field [e.g., *Wijesekera and Dillon*, 1997; *Gibson*, 1998] or the gradient Richardson number [*Baumert and Peters*, 2000], the overturn Froude number is generally of order 1 for all three passes.

4.1. Flux Richardson Numbers

[29] Estimates of the flux Richardson number can be generated from the independently estimated production and buoyancy flux profiles, yielding values on the order of 0.15 to 0.25. A single Ri_f value was calculated for each pass as the mean of individual Ri_f estimates taken at 1 psu intervals between 5 and 15 psu, where the shear and stratification are both generally linear. These values are plotted with respect to the overturn Froude number, and $\frac{\varepsilon}{\nu N^2}$ in Figures 14 and 15, respectively. A comparison

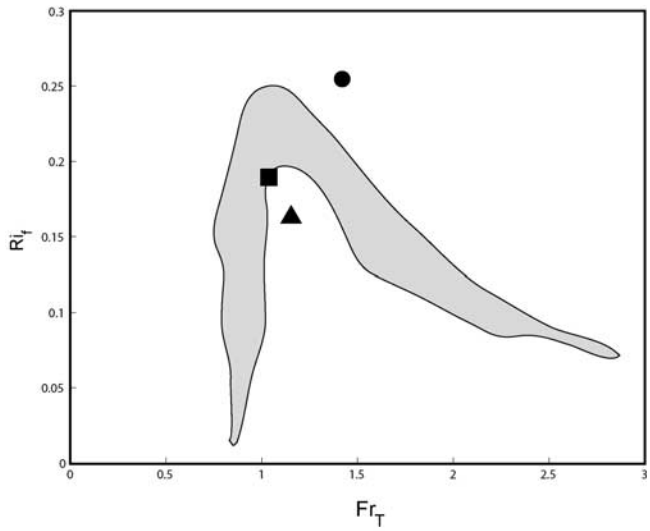

Figure 14. Mean values of the flux Richardson number (B/P) for each of the three passes, A, B, and C (represented by the circle, square, and triangle, respectively) plotted against the overturn Froude number. Points shown represent the mean of calculated values at isohalines from 5 to 15 psu. The shaded region represents the results of DNS simulations of a stratified shear flow for a variety of Prandtl numbers from 0.1 to 2.0, as described by *Ivey et al.* [1998, Figure 2].

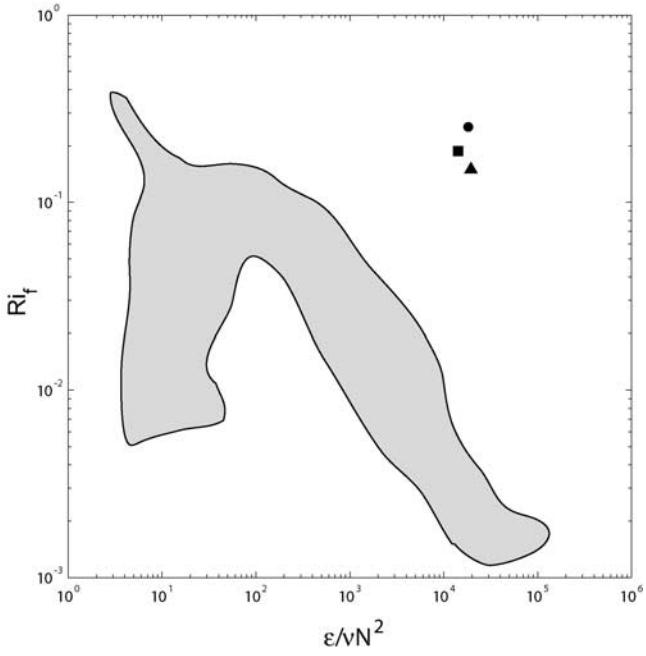

Figure 15. Mean values of the flux Richardson number (B/P) for each of the three passes, A, B, and C (represented by the circle, square, and triangle, respectively) plotted against $\varepsilon/\nu N^2$. Points shown represent the mean of calculated values at isohalines from 5 to 15 psu, as in Figure 14. Shaded region defines extent of data compiled by *Barry et al.* [2001b, Figure 7] representing the results of laboratory experiments using grid-generated turbulence. Data represented by the shaded region are drawn from *Stillenger et al.* [1983], *Rohr* [1985], *Itsweire et al.* [1987], and *Barry et al.* [2001b].

with Figure 6 also suggests that $Ri_f \approx Ri_g$, indicating that vertical eddy diffusivities for mass and momentum are equal [*Ellison*, 1957], consistent with a comparison of the vertical profiles of K_z^ρ and K_z^u in Figures 8 and 11.

[30] In Figure 14, values of Ri_f for the three passes are plotted against the overturn Froude number, and compared with the DNS results of *Ivey et al.* [1998]. The present results are generally consistent with the DNS simulations, as well as similar results shown by *Ivey and Imberger* [1991] which suggest that Ri_f should reach a maximum at a value of Fr_T equal to 1. However, in both of these previous data sets, values of $\frac{\varepsilon}{\nu N^2}$ on the order of those observed in the Fraser lift-off were only associated with much higher values of Fr_T, and consequently lower values of Ri_f. To illustrate this important distinction, the values of Ri_f associated with the present study are plotted against $\frac{\varepsilon}{\nu N^2}$ in Figure 15, and compared with data compiled by *Barry et al.* [2001b]. Here the present results are clearly inconsistent with the previous data sets, suggesting that high intensity grid-generated turbulence may not be directly comparable to larger scale shear stratified flows. The present results are also inconsistent with observations from regions where turbulence is generated by the breaking of internal waves not related to local shear [*Etemad-Shahidi and Imberger*, 2001]. The grid generated turbulence studied by *Barry et al.* [2001b] and others is characterized by Fr_T values on the order of 10 at $\frac{\varepsilon}{\nu N^2}$ values consistent with the Fraser data, so that the laboratory and numerical data occupy a different portion of the $Fr_T - \frac{\varepsilon}{\nu N^2}$ parameter space than the present data set, and, ultimately, no independent comparison to either parameter can adequately characterize the turbulent field. This reemphasizes the importance of the generating mechanism on the nature of the resulting turbulence, specifically with respect to the establishment of turbulent length scales.

[31] It should also be noted that high values of $\frac{\varepsilon}{\nu N^2}$ in the DNS simulations [i.e., *Ivey et al.*, 1998] and many of the laboratory grid experiments [i.e., *Barry et al.*, 2001a, 2001b] were driven by vanishingly small values of N^2. This results in Ozmidov scales that are larger than the length scales imposed on the problem by the numerical domain or tank size, which may limit the functional scale of the turbulence, effectively increasing the overturn Froude number, and driving Ri_f values down. In the Fraser liftoff region, and in many other geophysical examples of stratified shear turbulence [e.g., *Gargett and Moum*, 1995], N^2 is high, and high values of $\frac{\varepsilon}{\nu N^2}$ are driven by large dissipation rates.

4.2. Local Production Versus Advected TKE

[32] In order to determine whether the turbulence in the pycnocline might be explained by advection from the bottom boundary layer in the river channel, the magnitude of turbulent production in the bottom boundary layer and its advective contribution to the lift-off zone was assessed. Boundary layer shear production in the unstratified channel can be estimated assuming a log-layer shear profile as $P = \frac{u_*^3}{\kappa z}$, where u_* is a local shear velocity ($u_*^2 \approx C_d \bar{u}^2$, C_d is a bottom drag coefficient, taken as 3×10^{-3}), κ is von Karmans constant (equal to approximately 0.4), and z is the distance above the bed. This boundary layer production scale, on the order of 0.5×10^{-3} m^2 s^{-3}, is comparable to that observed within the stratified shear flow of the liftoff region.

[33] A length scale for the advection of this boundary layer turbulence can also be estimated by making an assumption that the observed production is balanced completely by advection, so that $P = u\frac{\partial u_*^2}{\partial x}$. This relationships yields an extinction length scale, $L_x = \frac{\kappa z}{\sqrt{C_d}}$, which, for a representative height above the bed of 2.5 m is on the order of 20 m. This is nearly 2 orders of magnitude smaller than the streamwise length scale of the lift-off region, indicating that the observed turbulent production could not have been advected seaward from the unstratified boundary layer. Thus the turbulence observed in the stratified shear layer must be produced locally.

4.3. Vertical Velocities

[34] An entrainment coefficient can be defined as the ratio of an entrainment velocity to a representative streamwise velocity. As defined by *Morton et al.* [1956] and *Ellison and Turner* [1959], the term entrainment refers to the rate of increase of streamwise volume flux within a turbulent region. With respect to the Fraser lift-off, the most appropriate depth at which to evaluate an entrainment velocity would be at the base of the plume, represented in this study by the 100% freshwater streamline, which is coincident with the 27 psu isohaline. Although the calculated values of w_h and w_j at the plume base are likely to be overestimated due to unresolved lateral flows, as described in Appendix B, they can be used to identify an appropriate scale for the

entrainment velocity on the order of 1 to 4×10^{-3} m s^{-1}. It should be noted that this entrainment velocity can be directly related to the maximum turbulent salt flux, $\overline{S'w'}$, which is observed higher in the water column, as a function of the vertical structure of the shear and density profiles. Assuming linear profiles of shear and density, it can be shown that the ratio $\frac{\overline{S'w'}_{max}}{S_o w_e}$ should be equal to a value of approximately 0.4, where S_o represents the salinity of the ambient seawater, and w_e is the entrainment velocity at the base of the plume. Using this relationship, and an observed maximum value of $B = g\beta\overline{S'w'}$ equal to approximately 2×10^{-4} m^2 s^{-3} (see Figure 8) a corresponding entrainment velocity would be equal to approximately 2.5×10^{-3}, which is consistent with the range suggested above.

[35] Given mean streamwise velocities in the upper layer of approximately 2 m s^{-1}, an appropriate entrainment coefficient, E, is of order 10^{-3}. *Ellison and Turner* [1959] suggested a dependence of the entrainment coefficient on a bulk Richardson number, $\frac{g'H}{U^2}$, where H is the plume depth and U is a representative plume velocity. Bulk Richardson numbers in the Fraser lift-off are on the order of 0.5 to 1, with an average value on the order of 0.7. Although the results of Ellison and Turner only represent flows with bulk Richardson numbers less than about 0.3, their data suggest a decreasing trend in E with increasing Ri_B, yielding entrainment coefficient values of order 10^{-2} at the upper end of their Ri_B range. Other data, compiled by *Christodoulou* [1986], extend the range of observations to values of the bulk Richardson number as high as 10^2, and suggest a value of the entrainment coefficient on the order of 10^{-3} for $Ri_B \sim 1$, which is consistent with the present observations.

[36] An earlier study of entrainment in the Fraser River plume [*Cordes et al.*, 1980] focused on a region of the plume extending approximately 40 km from Sand Heads (as opposed to 1 to 2 km in the present study). Their results suggested an entrainment rate on the order of 1 to 5×10^{-4}, roughly an order of magnitude lower than the value estimated in the present study. The data sets utilized by *Cordes et al.* [1980] could not be used to determine an accurate estimate of Ri_B, although later experiments by *Stronach* [1977] have suggested values of order 1 in similar regions of the plume. The entrainment coefficients of Cordes et al. suggest a value of Ri_B of approximately 2 or 3, based on the data compiled by *Christodoulou* [1986], which appears reasonable given the observed values of Ri_B in the first kilometer of the plume, and the associated deceleration of the plume at more significant distances from Sand Heads. The rapid transition and high momentum fluxes associated with plume lift-off in the first kilometer of the plume are responsible for driving more intense mixing processes, and lower values of Ri_B, than would be associated with the far-field, buoyancy driven plume.

[37] *Dallimore et al.* [2001] report entrainment coefficients for a saline underflow into a freshwater lake that range from 10^{-4} to 10^{-3} for Ri_B values on the order of 1. These are somewhat lower than the values observed in the Fraser, probably due to their calculation of E based on the turbulent transport of salt (i.e., $\overline{S'w'}$) rather than volume considerations as done here, and by *Ellison and Turner* [1959]. The results of *Dallimore et al.* [2001] are more directly comparable with the turbulent salt flux profiles generated in this study, which is undertaken in the following section.

[38] *Strang and Fernando* [2001] investigated entrainment rates across a sharp interface, with values of E approximately an order of magnitude larger at $Ri_B \sim 1$, than observed in this study. This discrepency can be explained by the natural adjustment of the turbulence field in the Fraser liftoff toward uniformly critical gradient Richardson numbers through a broadening of the mixed layer. Within this mixed layer the density profile exhibits a departure from the two-layer case (sharp interface) toward a more linearly stratified region, resulting in a significant decrease in Ri_B. For critical values of Ri_g, *Strang and Fernando* [2001] observed a value of E on the order of 10^{-3}, similar to the present study. In situations where flow conditions continuously adjust to maintain a broadening region of critical Ri_g, which appears to be the case in the Fraser lift-off, the entrainment coefficient would be approximately constant at the observed value.

4.4. Mechanisms of Turbulence Generation

[39] The most likely mechansim for the input of energy from the mean horizontal flow into turbulence is the generation of Kelvin-Helmholz billows through the propagation of shear instabilities. This is consistent with the observation of overturn Froude numbers close to unity, which is similar to several other large-scale field experiments [e.g., *Ferron et al.*, 1998]. The development and collapse of these instabilities in a laboratory flow similar to the Fraser lift-off is well described by *Pawlak and Armi* [2000].

[40] *Imberger and Ivey* [1991] indicate that the only two independent variables in a stratified shear flow are the shear, represented by Δu, and the stratification, which can be represented by g'. On the basis of the velocity and salinity observations shown in Figure 5, representative values of Δu and g' for the Fraser liftoff are approximately 2 m s^{-1}, and 0.15 m s^{-2}, respectively. Using these variables, and the definition of the gradient Richardson number, the gradient zone thickness, δ, can be expressed as $\delta = Ri_g\left[\frac{(\Delta u)^2}{g'}\right]$. The observed thickness of the gradient zone is consistent with this relationship, given the representative values of Δu and g', and a gradient Richardson number on the order of $\frac{1}{4}$.

[41] The ratio of the observed dissipation rate to a dissipation rate scaled from the independent variables, $(\Delta u g')$, is on the order of 2×10^{-3}. This ratio is proportional to an interfacial drag coefficient, C_{Di}, divided by the gradient Richardson number,

$$\frac{\varepsilon}{\Delta u g'} = \left(1 - Ri_f\right)\frac{C_{Di}}{Ri_g} = 2 \times 10^{-3}, \tag{12}$$

suggesting an interfacial drag coefficient on the order of 5×10^{-4}. Assuming a Prandtl number of 1, with $Ri_g \sim Ri_f$, C_{Di} is also equivalent to an alternative definition for the entrainment coefficient, $C_{Di} \sim \frac{\overline{\rho' w'}}{\Delta u \Delta \rho}$ [e.g., *Dallimore et al.*, 2001]. The value of 5×10^{-4} is in good agreement with similar observations made by *Dallimore et al.* [2001] of a saline underflow into a freshwater lake.

[42] These values represent the efficiency with which energy is extracted from the mean flow and converted into

turbulent energy, indicating that the turbulent energy is approximately 3 orders of magnitude lower than the mean flow energy. The values presented here may be representative of the processes involved in the generation of stratified-shear turbulence, but may not be constant. There may be a dependence of the drag coefficient on the bulk or gradient Richardson numbers, similar to the relationship that appears to hold for the entrainment coefficient [e.g., *Ellison and Turner*, 1959; *Christodoulou*, 1986]. Also, similarly to the flux Richardson number observations, these values may only be valid for overturn Froude numbers of order one, indicating turbulence generation through the formation of Kelvin-Helmholz instabilities.

[43] The stratified mixing generated within an estuarine outflow may also be dependent on larger-scale aspects of the plume structure, particularly limitations on lateral plume expansion due to local bathymetry or ambient conditions in receiving waters. Imposed limits on expansion would affect turbulent buoyancy flux through their influence on velocities within the plume. Under conditions where plume expansion is restricted, streamwise gradients of velocity within the plume will be reduced relative to an unconstrained plume. The rate of mixing within the plume may depend not only on the velocity difference within the plume, but also on the rate at which the velocity changes. Thus the geometry of the plume may influence the entrainment rate. The less of a lateral constraint, the more rapidly the plume accelerates, and the more intense the mixing would be within the pycnocline. The Fraser plume is partially constrained, both by the shoals to the south and the ambient southward flow. This may reduce the rate of mixing slightly from the value found in a plume with no lateral constraints.

[44] The net effect of these dynamic considerations may complicate predictions of TKE fluxes based solely on known river discharge and density differences. However, at local scales, it is likely that the formulation and value of the interfacial drag coefficient presented in equation (12) may well be representative of many similar stratified shear flows.

5. Conclusions

[45] This paper has presented a robust control volume approach for estimating TKE quantities in a stratified-shear flow. The resulting estimates of turbulent dissipation, on the order of 10^{-3} m^2 s^{-3}, with values of $\frac{\varepsilon}{\nu N^2}$ on the order of 10^4, are high compared to most other observations of dissipation in oceanic and coastal environments, and provide a good setting for the evaluation of turbulence energetics in a high-energy shear-stratified system. Observed flux Richardson numbers between 0.15 and 0.25 are consistent with less energetic laboratory and field observations where the overturn Froude number is of order one, and several other field studies at similar values of $\frac{\varepsilon}{\nu N^2}$. A scaling analysis based on the two independent variables in the system, Δu and g', suggests that entrainment and turbulent production may be well described through the use of entrainment and interfacial drag coefficients.

Appendix A: Reference Frames

[46] In a stratified flow, a natural reference frame for quantifying vertical transport is perpendicular to isopycnals [e.g., *Dallimore et al.*, 2001]. Similar motion can also be observed in unstratified conditions, such as entrainment into a turbulent jet [e.g., *Tennekes and Lumley*, 1972, pp. 127–132]. In this case the typical reference frame is a mean streamline bounding the initial fluid contained within the jet, or some volumetric subset of the initial jet. Assuming the receiving waters of a horizontally discharged buoyant plume are of constant density, the bounding edge of the plume must lie along an isopycnal, so that the entrainment velocity into the plume is independent of the reference frame imposed on the calculations. Within the interior of the plume, significant differences between the two reference frames would be observed depending on their respective orientation.

[47] Generically, a normal velocity can be defined as

$$\vec{w}_e = \vec{u} \cdot \vec{n}_e, \tag{A1}$$

where $\vec{w}_e$ represents the velocity across the surface defined by the normal unit vector $\vec{n}_e$, and $\vec{u}$ is the local velocity vector. We refer to two velocities, the diahaline velocity, $\vec{w}_h$, which represents entrainment across isohalines, and the "jet-entrainment" velocity, $\vec{w}_j$. Diahaline velocities can be of either sign depending on position in the water column, as a growing mixed layer must incorporate fluid from both directions if the layer is to grow. In order to conserve salt on an isohaline surface, all fluid crossing an isohaline must be diluted through mixing, indicating that the turbulent component of salt flux and the diahaline velocity are related processes [*McDougall*, 1984].

[48] The jet entrainment velocity represents entrainment into a region defined by a specified fraction of the original discharging fluid. In the case of a buoyant plume discharged at the surface, this implies that all jet entrainment velocities must be of the same sign, and directed upward. The simple diagrams in Figure A1 show the distinction between these two reference frames.

Appendix B: Lateral Effects

[49] In addition to measurement errors associated with the raw variables, a potential source of error to the control volume calculations is the lateral import or export of volume, salt and momentum. A separate analysis of data from the 2000 freshet, as discussed by *MacDonald* [2003], has suggested that the flow in this region of the channel is nearly two-dimensional, particularly above the 20 psu isohaline, based on a three-dimensional salt balance and the relative contribution of lateral (southward-directed) salt flux to the overall salt budget in the region. However, due to the complexities of the interactions between entrainment and turbulence in generating the vertical transport, there are multiple pathways through which lateral fluxes may impact the calculations. An estimate of the magnitude of the contributions of lateral flux to the overall volume, momentum, and salt budgets is, therefore, an important goal.

[50] These estimates can be obtained using the observed cross-stream velocity profile, and estimating a cross-channel length scale, l_C, which represents the distance to the channel boundary across which the lateral flow must decrease to

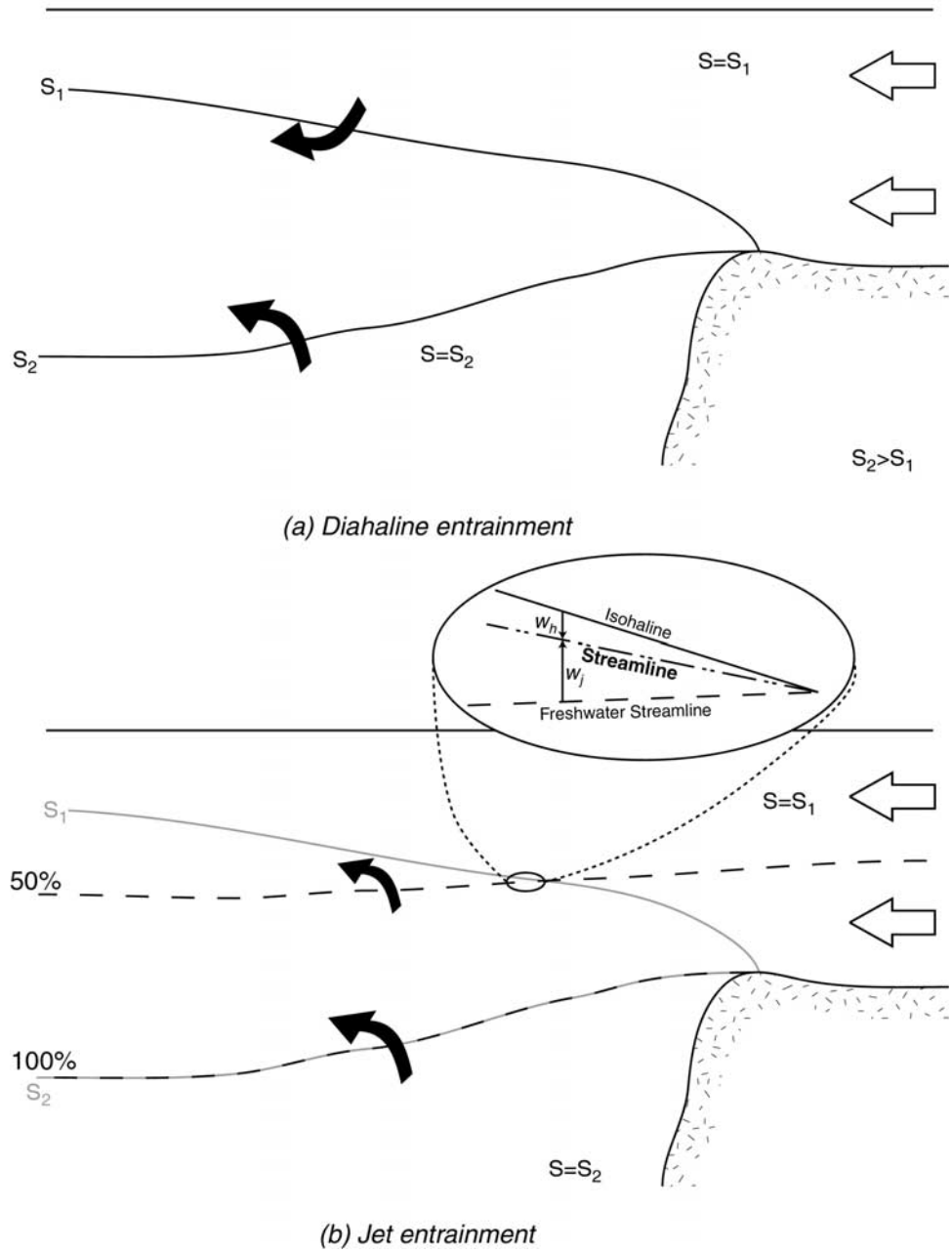

Figure A1. Cartoons of entrainment relative to (a) isohalines and (b) surfaces of constant initial discharge, where the dashed lines represent the bounding limits of the upper 50% and 100% of the initial discharge as it expands into the ambient fluid. In the first case, entrainment, as shown by the solid arrows, can be of opposite sign at different levels in the water column, resulting in mixed layer growth. In the second case, the sign of the entrainment is always positive. The inset in Figure A1b demonstrates that the entrainment velocity represents the vector difference between a mean streamline and a vector representation of the respective surface.

zero. A profile of lateral volume influx can be estimated by integrating the cross-stream velocity profile,

$$\hat{V}(h) = \int_{x_1}^{x_2} \int_{h}^{0} v\left(\frac{b}{l_c}\right) dz dx, \tag{B1}$$

where $\hat{V}$ represents the lateral volume influx, and v is the cross-stream velocity.

[51] The first panel of Figure B1 shows profiles of cross-stream velocity averaged across the control volume for each of the passes. In the second panel, the ratio of lateral volume influx to the maximum volume flux divergence across the control volume in the streamwise direction (in this case representing the lowest calculation point in the water column) is plotted. The curves in the second panel were generated using a depth dependent value of l_c based on local bathymetry. The cross-stream velocity

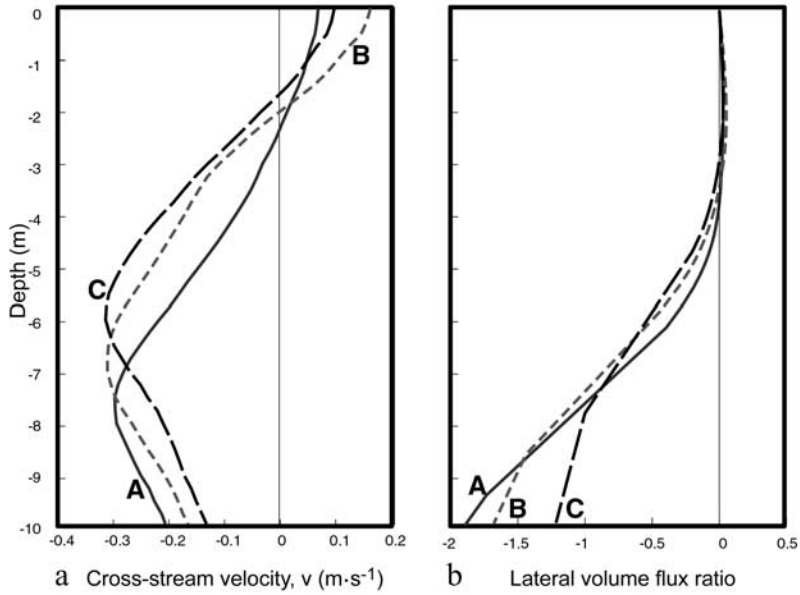

Figure B1. (a) Vertical profiles of the cross stream velocity, positive values directed to the right of the discharging flow (northward). (b) Profile of the estimated lateral volume flux to the maximum observed streamwise volume flux divergence, as described in Appendix B.

profiles in the first panel show relatively small and balanced velocities in the top 4 m of the water column, with more intense southward-directed velocities, approaching 30 cm s^{-1}, in the lower portion of the water column. It is the flux in this lower region that supplies most of the salt to the lift-off zone [*MacDonald*, 2003] and is most likely to influence the salt balance and thus impact the turbulence calculations.

[52] As expected, based on the velocity profiles in the first panel, the ratio in the second panel of Figure B1 increases rapidly below about 5 m, with errors that are generally negligible in the upper half of the water column.

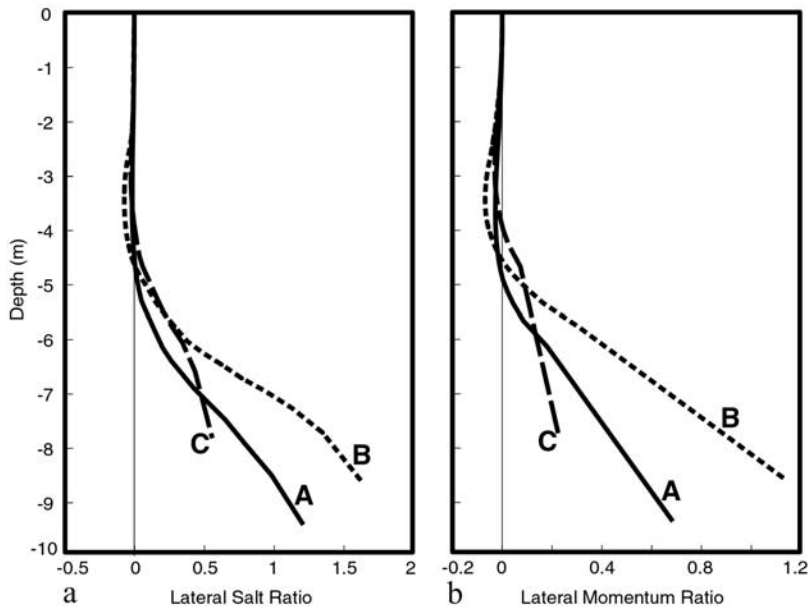

Figure B2. Lateral influx ratios for both (a) salt and (b) momentum. The ratios represent the cumulative effect of lateral influx (including both the direct lateral flux divergence of salt and streamwise momentum, and the indirect effect of lateral volume flux affecting entrainment estimates) divided by the maximum calculated values of $\overline{S'w'}$ (shown in Figure 8 as buoyancy flux) and $\overline{u'w'}$ (shown in Figure 10). Significant errors are identifiable in both cases in the lower portion of the water column below approximately 6 m depth, with the salt flux calculations more susceptible to lateral errors than the momentum calculations.

The negative sign of the ratio indicates that the calculated values of w_h and w_j are likely to be overestimated, and that velocities may begin to decrease below about 5 m rather than the monotonic increase suggested by the curves in Figure 7.

[53] Uncertainty in the value of the vertical entrainment velocity propagates into the turbulence flux estimates directly through the mean transport terms of equations (5) and (8), where it is amplified by the mean value of the transported quantity. Hence, potential errors in the lower portion of the water column due to errors in the vertical velocity are greatly amplified in the turbulent salt flux calculations due to the high value of salinity at depth. Similarly, errors are reduced in the momentum flux calculations due to the small along-channel velocities at depth.

[54] Additional errors are introduced to the turbulence calculations through the direct lateral flux of momentum and salt. These errors are typically of opposite sign to the entrainment related errors, reducing the overall impact of the lateral influx. Figure B2 presents plots similar to those shown in the second panel of Figure B1, showing the combined effect of both of these mechanisms (entrainment velocity errors induced by the lateral influx of volume, and the direct lateral flux of salt and momentum) on the salt and momentum budget calculations. These plots, combined with the curves presented in Figure B1, clearly indicate that a high degree of uncertainty is associated with all calculations at depths below approximately 5 to 6 m. Discussion in the main text is therefore limited to the upper region of the water column where errors associated with lateral fluxes are small.

[55] **Acknowledgments.** The authors thank David Jay, Philip Orton, and Alex Horner for their help during the field efforts. This work was performed as a part of D. MacDonald's Ph.D. thesis, and was funded by Office of Naval Research grants N000-14-97-10134 and N000-14-97-10566, National Science Foundation grant OCE-9906787, a National Science Foundation graduate fellowship, and support from the WHOI Academic Programs Office.

References

Balmforth, N. J., S. G. Llewellyn Smith, and W. R. Young (1998), Dynamics of interfaces and layers in a stratified turbulent fluid, *J. Fluid Mech.*, *355*, 329–358.

Barry, M. E., G. N. Ivey, K. B. Winters, and J. Imberger (2001a), Measurements of diapycnal diffusivities in stratified fluids, *J. Fluid Mech.*, *442*, 267–291.

Barry, M. E., G. N. Ivey, K. B. Winters, and J. Imberger (2001b), Laboratory experiments on diapycnal mixing in stratified fluids, paper presented at 12th 'Aha Huliko'a Hawaiian Winter Workshop "From Stirring to Mixing in a Stratified Ocean," Univ. of Hawaii, Honolulu.

Baumert, H., and H. Peters (2000), Second-moment closures and length scales for weakly stratified turbulent shear flows, *J. Geophys. Res.*, *105*(C3), 6453–6468.

Christodoulou, G. C. (1986), Interfacial mixing in stratified flows, *J. Hydraul. Res.*, *24*(2), 77–92.

Cordes, R. E., S. Pond, B. R. de Lange Boom, and P. H. LeBlond (1980), Estimates of entrainment in the Fraser River Plume, British Columbia, *Atmos. Ocean*, *18*(1), 15–26.

Dallimore, C. J., J. Imberger, and T. Ishikawa (2001), Entrainment and turbulence in saline underflow in Lake Ogawara, *J. Hydraul. Eng.*, *127*(11), 937–948.

Ellison, T. H. (1957), Turbulent transport of heat and momentum from an infinite rough plane, *J. Fluid Mech.*, *2*, 456–466.

Ellison, T. H., and J. S. Turner (1959), Turbulent entrainment in stratified flows, *J. Fluid Mech.*, *6*, 423–448.

Etemad-Shahidi, A., and J. Imberger (2001), Anatomy of turbulence in thermally stratified lakes, *Limnol. Oceanogr.*, *46*(5), 1158–1170.

Ferron, B., H. Mercier, K. Speer, A. Gargett, and K. Polzin (1998), Mixing in the Romanche Fracture Zone, *J. Phys. Oceanogr.*, *28*, 1929–1945.

Gargett, A. E., and J. N. Moum (1995), Mixing efficiencies in turbulent tidal fronts: Results from direct and indirect measurements of density flux, *J. Phys. Oceanogr.*, *25*, 2583–2608.

Geyer, W. R., and D. M. Farmer (1989), Tide-induced variation of the dynamics of a salt wedge estuary, *J. Phys. Oceanogr.*, *19*, 1060–1072.

Gibson, C. (1998), Intermittency of internal wave shear and turbulence dissipation, in *Physical Processes in Lakes and Oceans*, *Coastal Estuarine Stud.*, vol. 54, edited by J. Imberger, pp. 363–376, AGU, Washington, D. C.

Grant, H. L., R. W. Stewart, and A. Moilliet (1962), Turbulence spectra from a tidal channel, *J. Fluid Mech.*, *12*, 241–268.

Gregg, M. C. (1987), Diapycnal mixing in the thermocline: A review, *J. Geophys. Res.*, *92*(C5), 5249–5286.

Gregg, M. C. (1989), Scaling turbulent dissipation in the thermocline, *J. Geophys. Res.*, *94*(C7), 9686–9698.

Imberger, J., and G. N. Ivey (1991), On the nature of turbulence in a stratified fluid: II. Application to lakes, *J. Phys. Oceanogr.*, *21*, 659–680.

Itsweire, E. C., K. N. Helland, and C. W. Van Atta (1987), The evolution of grid-generated turbulence in a stably stratified fluid, *J. Fluid Mech.*, *162*, 299–338.

Ivey, G. N., and J. Imberger (1991), On the nature of turbulence in a stratified fluid: I. The energetics of mixing, *J. Phys. Oceanogr.*, *21*, 650–658.

Ivey, G. N., J. Imberger, and J. R. Koseff (1998), Buoyancy fluxes in a stratified fluid, in *Physical Processes in Lakes and Oceans*, *Coastal Estuarine Stud.*, vol. 54, edited by J. Imberger, pp. 377–388, AGU, Washington, D. C.

Kashiwamura, M., and S. Yoshida (1967), Outflow pattern of fresh water issued from a river mouth, *Coastal Engineering in Japan*, *10*, 109–115.

Kashiwamura, M., and S. Yoshida (1972), Flow pattern at a river mouth, paper presented at International Symposium on Stratified Flows, Am. Soc. of Civ. Eng., New York.

Kay, D. J., and D. A. Jay (2003a), Interfacial mixing in a highly stratified estuary: 1. Characteristics of mixing, *J. Geophys. Res.*, *108*(C3), 3072, doi:10.1029/2000JC000252.

Kay, D. J., and D. A. Jay (2003b), Interfacial mixing in a highly stratified estuary: 2. A "method of constrained differences" approach for the determination of the momentum and mass balances and the energy of mixing, *J. Geophys. Res.*, *108*(C3), 3073, doi:10.1029/2000JC000253.

Ledwell, J. R., A. J. Watson, and C. S. Law (1993), Evidence for slow mixing across the pycnocline from an open-ocean tracer-release experiment, *Nature*, *364*, 701–702.

MacDonald, D. G. (2003), Mixing processes and hydraulic control in a highly stratified estuary, Ph.D. thesis, Mass. Inst. of Technol./Woods Hole Oceanogr. Inst, Woods Hole.

McDougall, T. J. (1984), The relative roles of diapycnal and isopycnal mixing on subsurface water mass conversion, *J. Phys. Oceanogr.*, *14*, 1577–1589.

Morton, B. R., G. Taylor, and J. S. Turner (1956), Turbulent gravitational convection from maintained and instantaneous sources, *Proc. R. Soc. London, Ser. A*, *234*, 1–23.

Moum, J. N. (1996), Efficiency of mixing in the main thermocline, *J. Geophys. Res.*, *101*(C5), 12,057–12,069.

Osborn, T. R. (1980), Estimates of the local rate of vertical diffusion from dissipation measurements, *J. Phys. Oceanogr.*, *10*, 83–89.

Pardyjak, E. R., P. Monti, and H. J. S. Fernando (2002), Flux Richardson number measurements in stable atmospheric shear flows, *J. Fluid Mech.*, *459*, 307–316.

Pawlak, G., and L. Armi (2000), Mixing and entrainment in developing stratified currents, *J. Fluid Mech.*, *424*, 45–73.

Peters, H. (1999), Spatial and temporal variability of turbulent mixing in an estuary, *J. Mar. Res.*, *57*(6), 805–845.

Peters, H., M. C. Gregg, and J. M. Toole (1988), On the parameterization of equatorial turbulence, *J. Geophys. Res.*, *93*(C2), 1199–1218.

Rohr, J. J. (1985), An experimental study of evolving turbulence in uniform mean shear flows with and without stable stratification, Ph.D. thesis, Eng. Sci., Univ. of Calif., San Diego, La Jolla.

Stacey, M. T., S. G. Monismith, and J. R. Burau (1999), Measurements of Reynolds stress profiles in tidal flows, *J. Geophys. Res.*, *104*(C5), 10,933–10,949.

Stillenger, D. C., K. N. Helland, and C. W. Van Atta (1983), Experiments on the transition of homogeneous turbulence to internal waves in a stratified fluid, *J. Fluid Mech.*, *131*, 91–122.

Strang, E. J., and H. J. S. Fernando (2001), Entrainment and mixing in stratified shear flows, *J. Fluid Mech.*, *428*, 349–386.

Stronach, J. A. (1977), Observational and modelling studies of the Fraser River plume, Ph.D. thesis, Univ. of B. C., Vancouver, B. C., Canada.
Tennekes, H., and J. L. Lumley (1972), *A First Course in Turbulence*, MIT Press, Cambridge, Mass.
Thorpe, S. A. (1971), Experiments on the instability of stratified shear flows: Miscible fluids, *J. Fluid Mech.*, *46*, 299–319.
Thorpe, S. A. (1973), Experiments on instability and turbulence in a stratified shear flow, *J. Fluid Mech.*, *61*, 731–751.
Thorpe, S. A. (1977), Turbulence and mixing in a Scottish loch, *Philos. Trans. R. Soc. London, Ser. A*, *286*, 125–181.
Wijesekera, H. W., and T. M. Dillon (1997), Shannon entropy as an indicator of age for turbulent overturns in the oceanic thermocline, *J. Geophys. Res.*, *102*(C2), 3279–3291.
Wright, L. D., and J. M. Coleman (1971), Effluent expansion and interfacial mixing in the presence of a salt wedge, Mississippi River Delta, *J. Geophys. Res.*, *76*(36), 8649–8661.

W. R. Geyer, Department of Applied Ocean Physics and Engineering, MS 12, Woods Hole Oceanographic Institution, Woods Hole, MA 02543, USA. (rgeyer@whoi.edu)
D. G. MacDonald, School for Marine Science and Technology, University of Massachusetts–Dartmouth, 706 South Rodney French Boulevard, New Bedford, MA 02744-1221, USA. (dmacdonald@umassd.edu)